Interlaboratory Application of Raman CO2 Densimeter Equations: Experimental Procedure and Statistical Analysis Using Bootstrapped Confidence Intervals

DOI: 10.1177/0003702820987601

Inter-Laboratory Application of Raman CO_2 Densimeter Equations: Experimental Procedure and Statistical Analysis Using Bootstrapped Confidence Intervals

Journal:	*Applied Spectroscopy*
Manuscript ID	ASP-20-0304.R1
Manuscript Type:	Submitted Manuscript
Date Submitted by the Author:	20-Nov-2020
Complete List of Authors:	Remigi, Samantha; University of Milan–Bicocca, Department of Earth and Environmental Sciences Mancini, Tullio; University of Southampton, Department of Economic, Social and Political Science Ferrando, Simona; Università degli Studi di Torino, Dipartimento di Scienze della Terra Frezzotti, Maria Luce; Università degli Studi di Milano-Bicocca, Dipartimento di Scienze dell'Ambiente e della Terra
Manuscript Keywords:	Raman spectroscopy, Carbon dioxide, Raman densimeter equation, CO2 density
Abstract:	Raman spectroscopy has been used extensively to calculate CO2 fluid density in many geological environments, based on the measurement of the Fermi diad split (Δ; cm-1) in the CO2 spectrum. While recent research has allowed the calibration of several Raman CO2 densimeters, there is a limit to the inter-laboratory application of published equations. These calculate two classes of density values for the same measured Δ, with a deviation of 0.09 ± 0.02 g/cm3 on average. To elucidate the influence of experimental parameters on the calibration of Raman CO2 densimeters, we propose a bottom-up approach beginning with the calibration of a new equation, to evaluate a possible instrument-dependent variability induced by experimental conditions. Then, we develop bootstrapped confidence intervals for density estimate of existing equations to move the statistical analysis from a sample-specific to a population level. We find that Raman densimeter equations calibrated based on spectra acquired with similar spectral resolution calculate CO2 density values lying within standard errors of equations and are suitable for the inter-laboratory application. The statistical analysis confirms that equations calibrated at similar spectral resolution calculate CO2 densities equivalent at 95% confidence, and that each Raman densimeter does have a limit of applicability, statistically defined by a minimum Δ value, below which the error in calculated CO2 densities is too high.

Paper Type: *Submitted Paper*

Inter-Laboratory Application of Raman CO_2 Densimeter Equations: Experimental Procedure and Statistical Analysis Using Bootstrapped Confidence Intervals

Samantha Remigi[a,*], Tullio Mancini[b], Simona Ferrando[c], Maria Luce Frezzotti[a,*]

[a] Dipartimento di Scienze dell'Ambiente e della Terra, Università Milano–Bicocca, Piazza della Scienza 4, 20126, Milano, Italy

[b] Department of Economic, Social and Political Science, University of Southampton, University Road, SO17 1BJ, Southampton, United Kingdom

[c] Dipartimento di Scienze della Terra, Università di Torino, Via Valperga Caluso, 35, 10125, Torino, Italy

* Corresponding author emails: s.remigi@campus.unimib.it; maria.frezzotti@unimib.it

Abstract

Raman spectroscopy has been used extensively to calculate CO_2 fluid density in many geological environments, based on the measurement of the Fermi diad split (Δ; cm^{-1}) in the CO_2 spectrum. While recent research has allowed the calibration of several Raman CO_2 densimeters, there is a limit to the inter-laboratory application of published equations. These calculate two classes of density values for the same measured Δ, with a deviation of 0.09 ± 0.02 g/cm^3 on average. To elucidate the influence of experimental parameters on the calibration of Raman CO_2 densimeters, we propose a bottom-up approach beginning with the calibration of a new equation, to evaluate a possible instrument-dependent variability induced by experimental conditions. Then, we develop bootstrapped confidence intervals for density estimate of existing equations to move the statistical analysis from a sample-specific to a population level. We find that Raman densimeter equations calibrated based on spectra acquired with similar spectral resolution calculate CO_2 density values lying within standard errors of equations and are suitable for the inter-laboratory application. The statistical analysis confirms that equations calibrated at similar spectral resolution calculate CO_2 densities equivalent at 95% confidence, and each Raman densimeter

does have a limit of applicability, statistically defined by a minimum Δ value, below which the error in calculated CO_2 densities is too high.

Keywords

Raman spectroscopy, carbon dioxide, Raman densimeter equation, carbon dioxide density, CO_2

Introduction

Raman spectroscopy represents an attractive and popular technique to characterize a range of chemical and physical properties of Earth's fluids trapped as inclusions due to its nondestructive nature and high spatial resolution.[1–3] In particular, the calculation of the density of CO_2 fluids by Raman spectroscopy exploits the existing relation between the fluid density and the spectral position difference of the two main CO_2 bands in the Raman spectrum (Fig. 1a).[4–11]

Due to its linear symmetry, the CO_2 molecule is characterized by four vibrational modes: a symmetric stretching mode ν_1, an asymmetric stretching mode ν_3, and two bending modes $2\nu_{2a}$ and $2\nu_{2b}$ having the same vibrational frequencies. The symmetric stretching mode ν_1 has nearly the same energy and symmetry of the two bending modes $2\nu_2$. Thus, when activated, these become mutually repellent to one another and degenerate. This anharmonic coupling originates a vibrational resonance, known as "Fermi resonance" effect,[12] which results in the splitting apart of two bands ($\nu_1 - 2\nu_2$, defined as "Fermi diad"; Fig.1a), having frequencies at 1388.2 (upper band) and 1285.4 cm^{-1} (lower band), respectively, at ambient conditions.[13]

[insert: Figure 1]

Raman CO_2 densimeter equations formalize the linear relation between the Fermi diad split (Δ; cm^{-1}) and CO_2 density (d; g/cm^3).[11,14–19] These are empirically calibrated using CO_2 with known density calculated either by microthermometry of natural or synthetic fluid inclusions or using the equation of state (EOS) of CO_2 in optical pressure cells. Each densimeter equation is represented by a polynomial function, where the degree of the best fitting curve has been chosen based on the calculation of the root mean square error.[19,20] Although equations well fit descriptive statistics of data, published Raman densimeters calculate two distinct classes of density values for each Δ value measured in spectra, having a standard deviation of 0.09 ± 0.02 g/cm^3 on average (Fig. 1b). Each given CO_2 density value corresponds to Fermi diad splits showing an average wavenumber discrepancy of 0.2 cm^{-1} between the two classes of

densimeters.[14–19] As a result, the application of Raman CO_2 densimeter equations to measure the density of CO_2 fluids in inclusions is limited to single laboratories. This difficulty suggests an instrument-dependent source of variability and poses the question of the reliability of the equations.

In the present study, we calibrate a new equation using Raman spectra of CO_2 inclusions in mantle rocks. The new equation calculates densities consistent with Kawakami et al.[14] and Yamamoto and Kagi,[15] revealing a critical influence of the experimental parameters on spectra graphical output. An advanced statistic algorithm based on bootstrap[21] to calculate confidence interval is applied to evaluate the reliability of six CO_2 Raman densimeter polynomial equations, including the present study. Unknown data distributions, such as the Δd values, need robust statistical methods to move the analysis from a sample-specific level to a population setting, allowing generalization.

Present results demonstrate that densimeter equations calibrated applying a similar spectral resolution during Raman analysis calculate statistically equivalent density data at the 95% confidence. The bootstrap analysis extends the applicability of the densimeter equations to inter-laboratory analysis by defining a set of rules guiding practitioners on how to choose and use published Raman densimeter equations to calculate CO_2 fluid density in fluid inclusions.

Materials and Methods

To calibrate the Raman densimeter equation, we performed Raman and microthermometric analyses in pure CO_2 fluid inclusions in olivine and orthopyroxene of peridotite xenoliths from El Hierro (Canary Islands).[22] Inclusions are analyzed in double-polished rock sections of about 150 μm thickness.

Microthermometry

Microthermometry of fluid inclusions has been performed with a Linkam THM 600 heating-freezing stage system coupled with a Leitz petrographic microscope (40X objective) at the Università di Milano–Bicocca. The system has been daily calibrated based on the measurement of H_2O and CO_2 triple point temperatures (Tp), using synthetic fluid inclusion standards SYNFLINC, with an error of ± 0.1°C. The temperatures of CO_2 phase transitions have been recorded through several freezing-heating cycles, with heating rates variable from 0.1 to

0.5°C/min in the temperature intervals close to phase transitions. Measured homogenization temperatures both to the liquid (ThL) and vapor phase (ThV) have been used to calculate densities with the CO_2 equation of state proposed by Dusheck et al.,[23] with a standard error of ± 0.01 g/cm^3.

Raman Spectroscopy

Raman analyses have been performed with the Horiba Jobin Yvon LabRam HRVIS Raman System at the Centro "G. Scansetti", Dipartimento di Scienze della Terra, Università di Torino. The system is equipped with a Horiba Jobin Yvon HR800 spectrometer, connected to an air-cooled 1024*256 px charge-coupled device (CCD) detector, and provided with a wheel of six filters for laser attenuation and an Olympus BX41 microscope for petrographic observations in transmitted and reflected light. CO_2 spectra were recorded using a green Nd 532.06 nm laser source at 80 mW, with a 100X magnification. The experimental conditions consisted of a confocal hole of 200 µm, a slit width of 300 µm, and a 600 gr/mm grating, covering the spectral range between 105.35 and 1804.57 cm^{-1}, which correspond to a spectral resolution per pixel of 1.66 cm^{-1}. The Raman system has been further equipped with a Linkam THM 600 heating–freezing stage to analyze at a temperature (T) of 32<thinsp>°C (i.e., above the CO_2 critical *T* at 31.1<thinsp>°C) those inclusions characterized by the coexistence of vapor (V) and liquid (L) phases at room temperature (18<thinsp>°C). Inclusions' spectra have been acquired through cycles of three accumulations, from 20 to 40 seconds each.

Most Raman spectra have been duplicated by setting a similar Raman analytical setup with the Horiba Jobin Yvon LabRAM HR Evolution Raman System, at the Dipartimento di Scienze dell'Ambiente e della Terra, Università di Milano–Bicocca. The system has a focal length of 800 mm, and it is connected to an air-cooled 1024*256 px CCD detector and a wheel of nine neutral density filters. An Olympus BXFM microscope allows analyses in transmitted and reflected light. CO_2 spectra were recorded using a green Nd 532.06 nm laser source, powered at 150 mW by mean of the 50% neutral density filter, with a 100X magnification. The analytical set up consisted of a confocal hole of 100 µm and a 600 gr/mm grating, allowing the coverage of a spectral range between 101.35 and 1548.92 cm^{-1}, corresponding to a spectral resolution of about 1.40 cm^{-1}/px. Spectra have been acquired by one accumulation of 30 seconds each.

In both laboratories, analyses have been performed at constant room temperature (e.g., within 1<thinsp>°C interval). The calibration of the two Raman systems has been daily performed to the zero line (the laser line emission) with a synthetic diamond standard vibrating at 1331.82 cm^{-1}, according to the ASTM 1840–96 normative.[24,25] For the Raman system at the Università di Torino, the correction of the instrumental linearity[19,26] has been performed by additionally checking the main band of the silicon standard at 520.70 cm^{-1}. Measured drift between the silicon and diamond spectral region resulted in less than 1 cm^{-1}, and has been corrected by the adjustment of the Koeff. parameter in the LabSpec 5 software, as recommended by Lamadrid et al.[19] In the case of the spectrometers of the last generation, like the Raman system at the Università Milano–Bicocca, the correction of the instrumental linearity is automatically achieved by the automatic correction of the Koeff., by a sequential auto-calibration process to the zero line with the chosen standard in the CO_2 region (i.e., diamond; 1331.82 cm^{-1}).

With both instruments, the accuracy of the central band position attributions to monitor the variation of the band positions in Raman spectra as a function of the analyzed phases' physical–chemical characteristics, such as the fluid density, is in the order of 0.1 cm^{-1}.[27] For this reason, CO_2 spectra have been treated with baseline correction and band fitting with a Pseudo Voight function[28] by the freeware software Fityk 0.9.8.[29] The fitting allows improving the measurement accuracy up to 30 times.[15,30,31]

Bootstrapped Confidence Intervals

Five published CO_2 Raman densimeter polynomial equations[14–18] and the one proposed in the present study have been statistically evaluated by the computation of 95% confidence intervals of the fitted densities via the bootstrap approach. The linear equations of Rosso and Bodnar and Lamadrid et al.[11,19] have not been considered. The bootstrap algorithm, implemented in Rstudio 3.5.3, allowed computing the assumptions free 95% confidence intervals on the density estimates, enabling the analysis of the estimation accuracy of the different empirical equations and the statistical comparison among them.

The bootstrap[21] is a general nonparametric approach to statistical inference that allows constructing confidence limits on parameter estimates without assuming an underlying distribution. Among the different forms of bootstrapping – percentile bootstrap, time-series

bootstrap, and regression bootstrap – we focused on regression bootstrap to construct confidence intervals on the dependent variable. In particular, given the following relation (Eq. 1):

$$d_i = \beta_0 + \beta_1\Delta_i + \beta_2\Delta_i^2 + \beta_3\Delta_i^3 + \varepsilon_i \#(1)$$

the 95% confidence intervals for the estimated d will be produced.

The literature recognizes two general approaches to bootstrap (Eq. 1) by considering the covariates as either random or fixed.[32] The densities used in Eq. 1 are observed from the Δs computed by each equation. Being each equation specific for a certain set of Δ, it is assumed that the Δs are fixed observations. At the same time, the response variable has a random component arising from the error associated with each equation. Being this the case, the 95% confidence intervals of the response variable will be constructed using the residual bootstrapping, described below:[32]

Estimate the regression coefficients β_0, β_1, β_2, and β_3 from the observed values and compute the fitted values and residuals defined as:

$$\hat{d}_i = \hat{\beta}_0 + \hat{\beta}_1\Delta_i + \hat{\beta}_2\Delta_i^2 + \hat{\beta}_3\Delta_i^3$$

$$\varepsilon_i = d_i - \hat{d}_i$$

Sample with replacement the residuals from the original regression and compute the bootstrapped values of the response variable:

$$\boldsymbol{\varepsilon}_{\boldsymbol{b}}^* = [\varepsilon_{b1}^*, \varepsilon_{b1}^*, \ldots, \varepsilon_{bn}^*]'$$

Define $d_{bi}^* = \hat{d}_i + \varepsilon_{bi}^*$, and compute $\boldsymbol{d}_{\boldsymbol{b}}^* = [d_{b1}^*, d_{b2}^*, \ldots, d_{bn}^*]'$

Regress $\boldsymbol{d}_{\boldsymbol{b}}^*$ on the fixed regressors, and obtain the bootstrapped regression coefficients:

$$\boldsymbol{\beta}_{\boldsymbol{b}}^* = [\beta_{b0}^*, \beta_{b1}^*, \beta_{b2}^*, \beta_{b3}^*]$$

Points 1, 2, and 3 are repeated B times ($b \in [1;B]$) obtaining B coefficient estimates and, for each observation i, B bootstrapped prediction errors. For the scope of the paper, we will focus only on the construction of the 95% confidence intervals of the response variable. Once the B bootstrapped prediction errors are obtained, the 95% confidence intervals of the predicted response variable are constructed by selecting the 0.025 and 0.095 percentiles of the bootstrapped prediction errors and by adding these lower and upper bounds to each $\hat{d}_i$.
The 95% confidence interval (CI) is defined as a range of values that have been calculated from the data that, 95% of the time, includes the true value of the parameter, which is going to be estimated about the considered population.[33] This means that the CI could be used to provide a range of values that will contain the true population estimate.

In addition, a CI gives an indication of how precise the estimate is likely to be, with the margin of error as a measure of precision. If the CI is narrow, the margin of error is small; thus, the estimate is relatively precise; on the contrary, a wide CI implies a large margin of error; thus, the estimate has low precision.[33] Based on this, CI can be used to attribute the accuracy of the estimated fitted values and/or regressors coefficients.

The confidence interval can also be adopted to compare the estimation and predictive ability of two models: if the CIs for two models significantly overlap, then it constitutes an indication of (statistical) equivalence, at a given significance level, between the two.[34]
Finally, it is essential to highlight that, if the regression bootstrap allows constructing CIs without assuming an underlying distribution of the dependent variable, by keeping the Δ fixed, it assumes that:

The error terms are independent and identically distributed (IID), and consequentially when resampling we have Eq. 2:[35]

$$P\left(\varepsilon_{bi}^{*} = \varepsilon_i\right) = \frac{1}{n}, \quad \forall n = 1, \ldots, n \qquad (2)$$

which means that all the residuals have the same probability P to be randomly selected without any sampling biases.

The model in Eq. 1 is correctly specified.[32]

Results

Calibration of the Raman CO_2 Densimeter Equation

Selected CO_2 inclusions for the calibration of the Raman densimeter equation have prismatic to rounded shapes, and sizes ranging from 2 to 20 µm in diameter or length (Fig.1c and d; Table S1, Supplemental Material). Some inclusions have elongated prismatic shapes with widths not exceeding 1–1.5 µm. Depths location within the rock sections range from 8 to 43 µm, with most of the inclusions observed at depths comprised between 15 and 25 µm from the sample surface (Table S1).

Data Acquisition: Microthermometry and Raman Spectroscopy

The CO_2 melting temperatures (Tm) were recorded at –56.6 ± 0.1<thinsp>°C. Homogenization temperatures to the liquid phase (ThL) range from –32.5 to 31.0 ± 0.1<thinsp>°C. Two fluid inclusions homogenize to the vapor phase (ThV) at 30.5 ± 0.1 and 30.9 ± 0.1<thinsp>°C. Corresponding CO_2 densities are calculated with the equation of state of Dusheck et al.[23] and range from 0.37 to 1.08 ± 0.01 g/cm^3 (Table S1, Supplemental Material).

In Raman spectra of 40 pure fluid inclusions, CO_2 upper bands' central positions are distributed from 1386.42 to 1389.88 cm^{-1}, and lower bands' central positions between 1281.57 and 1286.11 cm^{-1} (Table S2). Based on the fitted center positions of the upper and lower CO_2 bands of acquired spectra, measured Δs vary from 103.44 to 105.13 cm^{-1} on increasing fluid density. Intensities of CO_2 upper bands are comprised between 110 and 9350 counts (in arbitrary units), with most values above 1000 counts. The lower band intensities are between 64 and 4688 counts (in arbitrary units), also in this case, with most values above 1000 counts. The band full widths at half-maximum (FWHM) range from 2.00 to 5.06 cm^{-1} for the upper bands, and from 2.20 to 4.80 cm^{-1} for the lower bands (Table S2).

For comparison, we measured the Fermi diad splits' distance in a few CO_2 spectra collected with a higher spectral per pixel resolution (i.e., 1800 gr/mm grating). We note that measured Δs resulted in being about 0.2 cm^{-1} greater on average (Figure S1, Supplemental Material).

Band Fitting Accuracy

The selection of CO_2 Raman bands to calibrate a densimeter equation is generally based on a minimum intensity value, selected between 500 and 1000 counts by the different authors.[14] The

accuracy of the central band position, however, is not only a function of band intensity (I) but also of its FWHM.[2,28] Therefore, for the present study, spectra selection for band best-fit has also been performed by considering the ratio between FWHM and I in single bands, defined as "band shape factor" (BSF = FWHM/I).

Calculated BSFs show a strong anticorrelation between band intensity and FWHM and vary from 0.0003 to 0.0349 for the CO_2 upper bands and from 0.0006 to 0.0545 for the lower bands (Table S2). The BSF plots relative to I (Figures 2a and b) graphically illustrate this relationship for the two CO_2 bands forming the Fermi doublet. In both diagrams, data plots define hyperbolic distributions, suggesting a minimum *I* over which and maximum FWHM below which the bands can be selected for best fit. The threshold values have been set at the points where the hyperboles invert their slopes (crossing red lines in Fig. 2a and b). The data plotting below the threshold values correspond to CO_2 upper bands (green field in Fig. 2a) having intensities ≥ 1000 counts and a BSF ≤ 0.004, and lower bands (green field in Fig. 2b) ≥ 600 counts and BSF ≤ 0.006. At higher BSF values, band intensities exponentially decrease with increasing FWHM for both the upper and lower bands, inducing an increase of uncertainty in central position assignment.

[insert: Figure 2]

It was expected that both the CO_2 upper bands and lower bands in the same spectrum would have similar BSF. Based on this approach, we removed 13 spectra from the database (Table S2). Unconsidered spectra were collected in CO_2 inclusions of density variable from 0.42 to 1.02 g/cm^3, excluding a correlation between BSF variability and fluid density. Conversely, these inclusions share several textural characteristics, including a location deeper than 25 μm within the sample, a size not exceeding 5 μm in length, and, often, an elongated shape (width of about 1–1.5 μm; Figs. 1c and d). Thus, one possible explanation is that confocal Raman spectroscopy analyses performed in tiny fluid inclusions located deep within the sample may have contributed to insufficient spectral output quality. The penetration profile for a laser source depends mainly on its wavelength, sample optical properties, and hole size,[2,36] and it decreases with increasing depth. For this reason, a small volume of a fluid located deep within the sample will be excited by the laser only to a lesser extent compared to the surrounding host mineral. As a consequence, the graphical resolution of spectra acquired beyond a certain depth would rapidly decrease.[27,30,36]

Calculation of CO_2 Densimeter Equation

The interpolation of the selected measured Δs and corresponding microthermometric densities (Table I) allows formulating an empirical third-order polynomial equation for the calculation of the CO_2 densities (Eq. 3):

$$d = -0.01472000\Delta^3 + 4.51148969\Delta^2 - 460.27795107\Delta + 15631.28847817 \quad (3)$$

with trend analysis determination coefficient, R^2, equal to 0.994. The resulting regression is shown in Fig. 3a.

[insert: Table I]

Equation 2 has been used to calculate the selected: for the considered Δ intervals, Raman densities resulted between 0.37 and 1.08 g/cm^3. Calculated CO_2 densities have an almost perfect positive correlation with microthermometric inclusions densities, with a mathematical expression (Eq. 4):

$$d_{micro.} = 1.0002(d_{Rd}) + 0.0027 \quad (4)$$

where $d_{micro.}$ are CO_2 densities derived from microthermometric measurements, and d_{Rd} those calculated using the Raman densimeter equation. The resulting regression is shown in Figure 3b, and it is characterized by a trend analysis determination coefficient equal to 0.994 and a standard error of ± 0.015 g/cm^3.

[insert: Figure 3]

As illustrated in Figure 3c, when plotted on a Δ versus *d* diagram, the present regression curve groups with Kawakami et al.[14] and Yamamoto and Kagi[15] ones, calculating CO_2 density values lying within the standard errors of the equations (σ = ± 0.015 g/cm^3) for density values equal or higher than 0.37 g/cm^3. Compared to Kawakami et al.[14] equation (K in Fig. 3c), it calculates densities that show a slight underestimation below 0.37 g/cm^3 (Δ*s* equal to 103.44 cm^{-1}, Fig.3c). The larger discrepancy is –0.03 g/cm^3. This minimal difference progressively decreases and remains within an interval of 0.01 g/cm^3 from 0.54 to 1.08 g/cm^3 (Δ between 103.76 and 105.13 cm^{-1}; Fig. 3c).

Again, when compared with the regression curve of Yamamoto and Kagi (Y in Fig. 3c),[15] the present equation shows the same slight density underestimation below 0.37 g/cm^3 (Δ*s* equal

to 103.44 cm^{-1}); progressively, the density difference decreases crossing Yamamoto and Kagi[15] value at 0.59 g/cm^3 (Δ of 103.86 cm^{-1}; Fig. 3c). For higher densities, the present densimeter calculates density values lying within the analytical error of Yamamoto and Kagi[15] equation. It reaches a maximum density difference of 0.03 g/cm^3 at 0.80 g/cm^3 (Δs equal to 104.33 cm^{-1}). The trend is reversed at 0.98 g/cm^3 (Δs equal to 104.81 cm^{-1}), where the density difference is 0.01 g/cm^3 at 1.08 g/cm^3 (Δs equal to 105.13 cm^{-1}; Fig. 3c).

Conversely, a robust disagreement is observed with the other set of densimeter equations, i.e., by Song et al., Fall et al., and Wang et al.[16–18] These equations calculate density values all lying well below those calculated by the present equation, with an average standard deviation of –0.09 ± 0.02 g/cm^3 in the whole range of considered densities.

Confidence Intervals of Raman Densimeter Equations

A bootstrap analysis was used to estimate confidence intervals of the predictions of density values of the six Raman densimeter equations considered in the present paper. The calibration data were selected from the original Δ and density data used by the different authors to calibrate densimeters.

[insert: Table II]

The empirical equations used for the bootstrap approach fit orthogonal polynomials as opposed to raw polynomials to reduce possible problems arising from the correlation among the different covariates.

The bootstrap analysis allows constructing the 95% confidence intervals from which it is possible not only to compare the different equations found in the literature but also to define a limit of applicability to each empirical regression. The cut-off point has been defined where the relative distances (between lower and upper limits) of the computed CIs are below than 7.5%. Above this threshold, the fitted density values are assumed not reliable due to the high variability coupled with the observed exponential increase. Figure 4 shows the computed thresholds and the densities variability in % for the six regressions. For Kawakami et al. (K in Fig. 4a),[14] Yamamoto and Kagi (Y in Fig. 4b),[15] and the present study (R in Fig. 4c) equations, the thresholds are located at Δs equal to 103.59, 103.59, and 103.44 cm^{-1}, respectively. These correspond to fitted densities of 0.46 g/cm^3 for Kawakami et al. and Yamamoto and Kagi,[14,15] and 0.37 cm^3 for the present study (Figs. 4 a–c). Above these fitted density values, most relative distances for the

three considered equations are < 5%. In the case of the empirical regressions of Kawakami et al. and Yamamoto and Kagi,[14,15] the calculated density variability below the threshold is above 30% (Fig. 4a and b). In the case of our equation, due to the considered dataset, no fitted densities fall above the threshold value (Fig. 4c).

[insert: Figure 4]

For the empirical regressions of Fall et al. (F in Figs. 4d), Wang et al. (W in Fig. 4e), and Song et al. (S in Fig. 4f),[16–18] the 7.5% thresholds correspond to Δs equal to 103.33, 103.53, and 103.45 cm^{-1}, respectively. The relative density values are 0.24 g/cm^3 for Fall et al., and 0.33 g/cm^3 for Wang et al. and Song et al.[16–18] equations (Figs. 4d–f). The relative errors before the thresholds exponentially increase for all the new equations, reaching the maximum variation of about 90% for Fall et al. (Fig. 4d), 60% for Wang et al. (Fig. 4e), and 15% for Song et al. (Fig. 4f)[16–18] equations.

Discussion

Influence of Experimental Procedure on the Calibration of Raman CO_2 Densimeter Equations

The present densimeter equation shows an excellent correlation with equations proposed by Kawakami et al.[14] and Yamamoto and Kagi (cf. Fig. 3c).[15] Measured Δs calculate CO_2 density values lying within the standard errors of the equations.

In these three laboratories, Raman spectra were collected at similar spectral resolution: 1.66 cm^{-1}/px for the present study, and 1.50 cm^{-1}/px for Kawakami et al. and Yamamoto and Kagi (cf., Table III).[14,15] In addition, as summarized in Table III, the applied experimental conditions include very similar spectrometer characteristics (i.e., the spectrometer focal length), the same CCD detector (1024*256 px) and diffraction grating (600 gr/mm), and very close laser source wavelengths (i.e., 532 nm for the present study, and 514 nm).[14,15]

We note that the spectral resolution applied to calibrate the other discrete group of Raman densimeter equations by Song et al., Fall et al., and Wang et al.[16–18] is also similar, but considerably higher, between 0.30 and 0.43 cm^{-1}/px.

[insert Table III]

In conclusion, we suggest that spectral resolution represents the prevailing experimental parameter affecting the Raman spectra of CO_2 fluids having the same density and, consequently, the observed differences among the two groups of densimeters.

A similar observation is entirely consistent with the fundamentals of Raman spectroscopy. The spectral resolution determines the Raman spectrometer's ability to measure, for example, the FWHM of a thin band or to discriminate between overlapping bands (e.g., number of points forming the bands).[27,41] Five main parameters generally define it: (i) the spectrometer focal length, (ii) the number of the pixels in the detector, (iii) the laser wavelength, (iv) the slit width, and (v) the diffraction grating. Among these, the diffraction grating is the most relevant one: the higher the number of grooves of the grating per mm, the higher the spectral resolution. When the spectral resolution is changed, both the band FWHM and I vary,[42] reflecting on the center position of the band in the spectral graphical output. Thus, on fitting, bands obtained with a higher spectral resolution would show a lower shift of center positions than those obtained with a lower spectral resolution. Since the distance of band center positions depend on the spectra graphical output, the shift is constant for the all Δ values.

Statistical comparison of existing densimeters based on bootstrapped confidence intervals The bootstrapping analysis predicts that Raman densimeter equations are not reliable to calculate CO_2 densities in the intervals where the relative distances of predicted CI are higher than 7.5% due to lower precision of fit. We note a general trend for each Raman densimeter equation best-fit dependent on the spectral resolution set to perform analyses. Predicted minimum density values to be considered reliable measurements are higher for those equations calibrated on Raman spectra acquired at medium spectral resolution conditions. Owing to this observation, we performed a statistical comparison of the new datasets independent regressions (cf. Confidence Intervals of Raman Densimeter Equations section above).[34] The distances of the Fermi diad split measured by one group of authors have been used to calculate CO_2 densities using the empirical regression estimated from the densities computed by another group of authors and successively compared with their CIs (Figs. 5 and 6). As an example, the Δs measured by Kawakami et al.[14] have been used to predict densities with the regression of Yamamoto and Kagi;[15] the resulting fitted density regression curve has been plotted against the CIs of Kawakami et al. (Fig. 5b).[14] If the fitted values fall inside the 95% confidence intervals, one can conclude that the two equations are statistically equivalent at 95% confidence. To test and evaluate the influence of the analytical conditions on the calibration of densimeter equations, the comparison was performed among equations resulting from Raman spectra collected with similar experimental conditions.

[insert: Figure 5]

`The comparison between fitted densities and confidence intervals,[34] shows an overlap of the 95% CIs between Kawakami et al., Yamamoto and Kagi[14–15] and the present study equations (Figs. 5a–c). This result indicates that these three "medium spectral resolution" equations are statistically equivalent at 95% of confidence. As illustrated in Fig. 5d, the statistical equivalence is limited to the range of the computed densities on which the equations are calibrated. Outside these ranges of density values, the proposed equations are no longer statistically equivalent.

[insert: Figure 6]

The comparison between Fall et al., Wang et al., and Song et al.[16–18] calculated densities and CIs,[34] shows at 95% confidence that also "high spectral resolution" equations are statistically equivalent in the density interval comprised between 0.33 and 1.00 g/cm^3 (Figs. 6a–c). Conversely, the statistical analysis shows that equations calibrated using different Raman spectral resolutions, are not statistically equivalent (Figs. 6d–f).

Thus, the bootstrap analysis provides a guide to select a CO_2 densimeter equation based on the applied experimental procedure. For spectra collected with a spectral resolution of 1.50 – 1.66 cm^{-1}/px, and for density values between 0.46 and 1.22 g/cm^3 (Δ from 103.59 to 105.81 cm^{-1}), any equation among those of Kawakami et al., Yamamoto and Kagi[14,15] and the present study could be used to calculate CO_2 densities with a confidence of 95% that the fitted values will be statistically equivalent. Also, the equation proposed in the present study can be applied for the density interval between 0.37 and 1.08 g/cm^3 (Δ from 103.44 to 105.13 cm^{-1}). Conversely, when a spectral resolution of 0.30 – 0.43 cm^{-1}/px is applied, Fall et al., Wang et al., and Song et al.[16–18] densimeter equations should be used to calculate CO_2 densities with a confidence of 95% that the fitted values will be statistically equivalent.

Applicability of Raman CO_2 Densimeter Equations

The present results suggest no strong reason to avoid the inter-laboratory adoption of published Raman densimeter equations to calculate densities of CO_2 fluid inclusions once the spectral resolution (cm^{-1}/px) applied during analyses is considered. A firm agreement in calculated density values is observed within the two groups of equations, calibrated at high and medium spectral resolutions, and could be regarded as a reliable measurement for comparison. The statistical analysis further predicts that each Raman CO_2 densimeter equation does have a limit of applicability, statistically defined by a minimum Δ value, below which the error in calculated

densities is too high. The minimum statistically accurate density values (< 7.5% *CI*) are different for each considered equation; they vary from 0.46 to 0.37 g/cm^3, and from 0.33 to 0.24 g/cm^3, depending on the spectral resolution applied and the interval of data considered (Fig. 4). The error exponentially increases at lower density values, standing above 20% at about 0.20 g/cm^3 for all equations (Fig. 4).

Minimum statistically accurate density values correspond to CO_2 fluids homogenizing to the vapor phase (ThV; $L+V \rightarrow V$) at temperatures variable from 31.0 to 30.0<thinsp>°C, and 29.6–24.8<thinsp>°C, close to the critical point of CO_2 (P = 7.38 MPa; T = 31.1<thinsp>°C) (Figure S2). Therefore, the simulated increasing trend of error could reflect a considerably lower accuracy of ThV measurements performed to calibrate the equations.[43] The "apparent homogenization phenomenon", proposed by Sterner[44] to highlight the underdetermination of phase transitions in fluid inclusions homogenizing by vapor expansion can induce an error as high as 0.10–0.30 g/cm^3 in calculated CO_2 densities.

An applicability limit, however, also applies to those densimeter equations calibrated based on measurements in optical gas cells, where CO_2 density is not determined by phase transitions.[45] In addition, it is evident that "high spectral resolution" densimeter equations calculate minimum statistically reliable density values that are lower than those of "medium spectral resolution" ones. Thus, other factors affecting the calibration of densimeter equations should be considered. In Raman spectra of CO_2, the position and width of the bands are a function of the molecular forces dominating the fluid volumes at different states and variable P–T conditions.[46–49] Consequently, not only the Fermi diad split (Δ) but also band intensity (I) and width (FWHMs) correlate with the fluid density.[4–11] Band line shape is also essential but seldom discussed characteristics that could influence the determination of band intensity, central position, and area. Based on ab initio calculations, Cabaço et al.[47] reported some discrepancies between observed and theoretically expected CO_2 band central positions resulting from the variation of band profiles with fluid density. In the case of high-density liquid-like CO_2 (e.g., d = 1.2–0.5 g/cm^3), authors reported a progressive symmetric broadening of the upper and lower bands with increasing fluid density, allowing the accurate measurement of CO_2 bands' central positions. Conversely, below the critical density, gas-like (d = 0.34 g/cm^3) CO_2 narrower bands showed progressively increasing asymmetric profiles, resulting in more challenging to obtain a sufficiently accurate fitting of central positions. Although further investigation is required, it is

probable that growing asymmetry of band profiles in spectra of low-density CO_2 could affect the accuracy of the band fitting, and hence of the calculated density values.

Conclusion

The present study demonstrates the possibility of inter-laboratories application of Raman densimeter equations to calculate the CO_2 density in fluid inclusions. A set of comments guiding the practitioners on how to choose and use a Raman densimeter equation to allow that the fitted values will be statistically equivalent at 95% confidence, includes: (i) The selected Raman CO_2 densimeter equation should be calibrated with the same (or similar) spectral resolution conditions. (ii) The selected Raman CO_2 densimeter equation should be applied only within the range of the density dataset used to calibrate the equation. (iii) The selected Raman CO_2 densimeter equation should be further applied limited to the interval of CO_2 density lying above a minimum reliable density value predicted by the bootstrapping, corresponding to a cut-off point where the relative distances of the computed CIs are lower than 7.5%.

One main consequence of present results is that the Raman densimeter method could potentially be applied to calculate CO_2 densities near and above the critical density value, which encompass P–T conditions relevant for most geological processes in the crust and the mantle. We believe that this method could become a more widespread analytical tool in the study of Earth's fluids in the near future and with the proposed improvements. On the contrary, the present results suggest caution in applying the Raman densimeters to CO_2 mass calculation in shrinkage bubbles of melt inclusions. Here, CO_2 has a considerably lower density, in the range from 0.02 to 0.30 g/cm^3,[50–53] in most cases below the minimum reliable density value predicted by our statistical analysis.

Acknowledgments

The present work is part of the Ph.D. thesis of S.R. This research was funded by MIUR projects to M.L.F.: PRIN 2017 (n. 2017LMNLAW) and Dipartimenti di Eccellenza (2018–2022). S.F. acknowledges the support of the University of Torino–Ricerca locale 2018 and 2019, and of the ANVUR–Fondo Finanziamento delle Attività Base di Ricerca. Raman analytical facilities in Torino were provided by the Interdepartmental Centre "G. Scansetti" for Studies on Asbestos and Other Toxic Particulates and by the Compagnia di San Paolo, Torino. Raman analytical

facilities in Milano–Bicocca were provided by The Dipartimento di Scienze dell'Ambiente e della Terra.

Declaration of Conflicting Interests

The Authors declare that there is no conflict of interests.

References

1. M.L. Frezzotti, S. Ferrando, F. Tecce, D. Castelli. "Water Content and Nature of Solutes in Shallow-Mantle Fluids from Fluid Inclusions". Earth Planet. Sci. Lett. 2012. 351: 70–83. https://doi.org/10.1016/j.epsl.2012.07.023
2. M.L. Frezzotti, F. Tecce, A. Casagli. "Raman Spectroscopy for Fluid Inclusion Analysis". J. Geochem. Explor. 2012b. 112: 1–20. https://doi.org/10.1016/j.gexplo.2011.09.009
3. R.J. Bodnar, M.L. Frezzotti. "Micro-Scale Chemistry: Raman Analyses of Fluid and Melt Inclusions". Elements. 2020. 16(2): 93–98. https://doi.org/10.2138/gselements.16.2.93
4. C.G. Gray, J.V. Kranendonk. "Calculation of the Pressure Broadening of Rotational Raman Lines Due to Multipolar and Dispersion Interaction". Can. J. Phys. 1966. 44(10): 2411–2430. https://doi.org/10.1139/p66-197
5. C.H. Wang, R.B. Wright. "Effect of Density on the Raman Scattering of Molecular Fluids. I. A Detailed Study of the Scattering Polarization, Intensity, Frequency Shift, and Spectral Shape in Gaseous N_2". J. Chem. Phys. 1973. 59(4): 1706–1712. https://doi.org/10.1063/1.1680252
6. Y. Garrabos, R. Tufeu, B. Le Neindre, G. Zalczer, D. Beysens. "Rayleigh and Raman Scattering Near the Critical Point of Carbon Dioxide". J. Chem. Phys. 1980. 72(8): 4637–4651. https://doi.org/10.1063/1.439706
7. J.F. Bertrán. "Study of the Fermi Doublet $\nu1–2\nu_2$ in the Raman Spectra of CO_2 in Different Phases". Spectrochim. Acta, Part A. 1983. 39(2): 119–121. https://doi.org/10.1016/0584-8539(83)80066-x
8. Y. Garrabos, V. Chandrasekharan, M.A. Echargui, F. Marsault-Herail. "Density Effect on the Raman Fermi Resonance in the Fluid Phases of CO_2". Chem. Phys. Lett. 1989a. 160(3): 250–256. https://doi.org/10.1016/0009-2614(89)87591-8

9. Y. Garrabos, M.A. Echargui, F. Marsault-Herail. “Comparison Between the Density Effects on the Levels of the Raman Spectra of the Fermi Resonance Doublet of the $^{12}C^{16}O_2$ and $^{13}C^{16}O_2$ Molecules”. J. Chem. Phys. 1989b. 91(10): 5869–5881. https://doi.org/10.1063/1.457455

10. J.C. Seitz, J.D. Pasteris, I.M. Chou. “Raman Spectroscopic Characterization of Gas Mixtures; I, Quantitative Composition and Pressure Determination of CH_4, N_2, and Their Mixtures”. Am. J. Sci. 1993. 293(4): 297–321. https://doi.org/10.2475/ajs.293.4.297

11. K.M. Rosso, R.J. Bodnar. “Microthermometric and Raman Spectroscopic Detection Limits of CO_2 in Fluid Inclusions and the Raman Spectroscopic Characterization of CO_2”. Geochim. Cosmochim. Acta. 1995. 59(19): 3961–3975. https://doi.org/10.1016/0016-7037(95)94441-h

12. E. Fermi. “Über den Ramaneffekt des Kohlendioxyds”. Z. Phys. 1931. 71(3–4): 250–259.

13. H.R. Gordon, T.K. McCubbin. “The 2.8 Micron Bands of CO_2”. J. Mol. Spectrosc. 1966. 19(1–4): 137–154. https://doi.org/10.1016/0022-2852(66)90237-2

14. Y. Kawakami, J. Yamamoto, H. Kagi. “Micro-Raman Densimeter for CO_2 Inclusions in Mantle-Derived Minerals”. Appl. Spectrosc. 2003. 57(11): 1333–1339. https://doi.org/10.1366/00037020322554473

15. J. Yamamoto, H. Kagi. “Extended Micro-Raman Densimeter for CO_2 Applicable to Mantle-Originated Fluid Inclusions”. Chem. Lett. 2006. 35(6): 610–611. https://doi.org/10.1246/cl.2006.610

16. Y. Song, I.M. Chou, W. Hu, B. Robert, W. Lu. “CO_2 Density-Raman Shift Relation Derived from Synthetic Inclusions in Fused Silica Capillaries and its Application”. Acta Geol. Sin. 2009. 83(5): 932–938. https://doi.org/10.1111/j.1755-6724.2009.00090.x

17. A. Fall, B. Tattitch, R.J. Bodnar. “Combined Microthermometric and Raman Spectroscopic Technique to Determine the Salinity of H_2O–CO_2–NaCl Fluid Inclusions Based on Clathrate Melting”. Geochim. Cosmochim. Acta. 2011. 75(4): 951–964. https://doi.org/10.1016/j.gca.2010.11.021

18. X. Wang, I.M. Chou, W. Hu, R.C. Burruss, et al. “Raman Spectroscopic Measurements of CO_2 Density: Experimental Calibration with High-Pressure Optical Cell (HPOC) and Fused Silica Capillary Capsule (FSCC) with Application to Fluid Inclusion

Observations". Geochim. Cosmochim. Acta. 2011. 75(14): 4080–4093. https://doi.org/10.1016/j.gca.2011.04.028

19. H.M. Lamadrid, L.R. Moore, D. Moncada, J.D. Rimstidt, et al. "Reassessment of the Raman CO_2 Densimeter". Chem. Geol. 2017. 450: 210–222. https://doi.org/10.1016/j.chemgeo.2016.12.034
20. Y. Hagiwara, J. Torimoto, J. Yamamoto. "Pressure Measurement and Detection of Small H_2O Amounts in High-Pressure H_2O–CO_2 Fluid Up to 141 MPa Using Fermi Diad Splits and Bandwidths of CO_2". J. Raman Spectrosc. 2020. 51(6): 1003–1018. https://doi.org/10.1002/jrs.5865
21. B. Efron. "Bootstrap Methods: Another Look at the Jackknife". Ann. Stat. 1979. 7(1): 1–26. https://www.jstor.org/stable/2958830
22. E. Oglialoro, M.L. Frezzotti, S. Ferrando, C. Tiraboschi, et al. "Lithospheric Magma Dynamics Beneath the El Hierro Volcano, Canary Islands: Insights from Fluid Inclusions". Bull. Volcanol. 2017. 79(10): 70. https://doi.org/10.1007/s00445-017-1152-6
23. W. Duschek, R. Kleinrahm, W. Wagner. "Measurement and Correlation of the (Pressure, Density, Temperature) Relation of Carbon Dioxide II. Saturated-Liquid and Saturated-Vapor Densities and the Vapor Pressure Along the Entire Coexistence Curve". J. Chem. Thermodyn. 1990. 22(9): 841–864. https://doi.org/10.1016/0021-9614(90)90173-n
24. ASTM International. ASTM E1840–96: Standard Guide for Raman Shift Standards for Spectrometer Calibration. https://www.astm.org/Standards/E1840.htm [accessed Dec 22 2020].
25. D. Hutsebaut, P. Vandenabeele, L. Moens. "Evaluation of an Accurate Calibration and Spectral Standardization Procedure for Raman Spectroscopy". Analyst. 2005. 130(8): 1204–1214. https://doi.org/10.1039/b503624k
26. F. Lin, A. K. Sum, R. J. Bodnar. "Correlation of Methane Raman ν1 Band Position with Fluid Density and Interactions at the Molecular Level". J. Raman Spectrosc. 2007. 38(11): 1510–1515. https://doi.org/10.1002/jrs.1804
27. J. Dubessy, M.C. Caumon, F. Rull, S. Sharma. "Instrumentation in Raman Spectroscopy: Elementary Theory and Practice". In: J. Dubessy, M.C. Caumon, F. Rull, editors. Raman Spectroscopy Applied to Earth Sciences and Cultural Heritage. London: European

Mineralogical Union and the Mineralogical Society of Great Britain and Ireland, 2012. Vol. 12, Chap. 3, Pp. 83–172. https://hal.univ-lorraine.fr/hal-01342830

28. X. Yuan, R.A. Mayanovic. "An Empirical Study on Raman Peak Fitting and its Application to Raman Quantitative Research". Appl. Spectrosc. 2017. 71(10): 2325–2338. https://doi.org/10.1177/0003702817721527
29. M. Wojdyr. "Fityk: A General-Purpose Peak Fitting Program". J. Appl. Cryst. 2010. 43: 1126–1128. https://doi.org/10.1107/s0021889810030499
30. S. Fukura, T. Mizukami, S. Odake, H. Kagi. "Factors Determining the Stability, Resolution, and Precision of a Conventional Raman Spectrometer". Appl. Spectrosc. 2006. 60(8): 946–950. https://doi.org/10.1366/000370206778062165
31. J. Yamamoto, H. Kagi, Y. Kawakami, N. Hirano, M. Nakamura. "Paleo-Moho Depth Determined from the Pressure of CO_2 Fluid Inclusions: Raman Spectroscopic Barometry of Mantle- and Crust-Derived Rocks". Earth Planet. Sci. Lett. 2007. 253(3–4): 369–377. https://doi.org/10.1016/J.Epsl.2006.10.038
32. J. Fox. "Bootstrapping Regression Models. Appendix to an R and S-PLUS Companion to Applied Regression". In: J. Fox, editor. An R and S-PLUS Companion to Applied Regression. Thousand Oaks, CA: Sage Publications, 2002.
33. G. Cumming, R. Calin-Jageman. Introduction to the New Statistics: Estimation, Open Science, and Beyond. New York: Routledge, 2016
34. M. Kuhn, K. Johnson. Applied Predictive Modelling. New York: Springer, 2013.
35. N. Balakrishnan, W. Chen. CRC Handbook of Tables for Order Statistics from Inverse Gaussian Distributions with Applications. New York: Routledge, 2017
36. E.A. Burke. "Raman Microspectrometry of Fluid Inclusions". Lithos. 2001. 55(1–4): 139–158. https://doi.org/10.1016/s0024-4937(00)00043-8
37. S.M. Sterner, R.J. Bodnar. "Synthetic Fluid Inclusions. X: Experimental Determination of P–V–T–X Properties in the CO_2–H_2O System to 6 Kb and 700<thinsp>°C". Am. J. Sci. 1991. 291(1): 1–54. https://doi.org/10.2475/ajs.291.1.1
38. KS. Pitzer, S. M. Sterner. "Equations of State Valid Continuously from Zero to Extreme Pressures for H_2O and CO_2". J. Chem. Phys. 1994. 101(4), 3111–3116. https://doi.org/10.1063/1.467624

39. S. Angus, B. Armstrong, K.M. de Reuck. “Carbon Dioxide: International Thermodynamic Tables of the Fluid State, Bd. 3”. In: S. Angus, B. Armstrong, K.M. de Reuck, editors. Pure and Mixed Refrigerants. Oxford; New York: Pergamon Press Ltd., 1976.

40. R. Span, W. Wagner. “A New Equation of State for Carbon Dioxide Covering the Fluid Region from the Triple-Point Temperature to 1100 K at Pressures Up to 800 Mpa”. J. Phys. Chem. Ref. Data. 1996. 25(6): 1509–1596. https://doi.org/10.1063/1.555991

41. F. Adar. “Raman Microscopy Analysis of Molecular Orientation in Organic Fibers”. Spectroscopy. 2013. 28(2): 14–22.

42. C.K. Mann, T.J. Vickers. “Instrument-to-Instrument Transfer of Raman Spectra”. Appl. Spectrosc. 1999. 53(7): 856–861. https://doi.org/10.1366/0003702991947441

43. E. Roedder. “Fluid Inclusions”. In: P.H. Ribbe, editor. Chantilly: Mineralogical Society of America (MSA), 1984. 12.

44. S.M. Sterner. “Homogenization of Fluid Inclusions to the Vapor Phase: The Apparent Homogenization Phenomenon”. Econ. Geol. 1992. 87(6): 1616–1623. https://doi.org/10.2113/gsecongeo.87.6.1616

45. T. Kobayashi, J. Yamamoto, T. Hirajima, H. Ishibashi, et al. “Conformity and Precision of CO2 Densimetry in CO_2 Inclusions: Microthermometry Versus Raman Microspectroscopic Densimetry”. J. Raman Spectrosc. 2012. 43(8), 1126–1133. https://doi.org/10.1002/jrs.3134

46. H. Nakayama, K.I. Saitow, M. Sakashita, K. Ishii, K. Nishikawa. “Raman Spectral Changes of Neat CO_2 Across the Ridge of Density Fluctuation in Supercritical Region”. Chem. Phys. Lett. 2000. 320(3–4): 323–327. https://doi.org/10.1016/s0009-2614(00)00249-9

47. M.I. Cabaço, S. Longelin, Y. Danten, M. Besnard. “Local Density Enhancement in Supercritical Carbon Dioxide Studied By Raman Spectroscopy”. J. Phys. Chem. A. 2007. 111(50): 12966–12971. https://doi.org/10.1021/jp0756707

48. M.I. Cabaço, M. Besnard, S. Longelin, Y. Danten. “Evolution with the Density of CO_2 Clustering Studied By Raman Spectroscopy”. J. Mol. Liq. 2010. 153(1): 15–19. https://doi.org/10.1016/j.molliq.2009.09.007

49. D.M. Sublett Jr., E. Sendula, H. Lamadrid, M. Steele-Macinnis, et al. “Shift in the Raman Symmetric Stretching Band of N_2, CO_2, and CH_4 as a Function of Temperature, Pressure, and Density”. J. Raman Spectrosc. 2020. 51(3): 555–568. https://doi.org/10.1002/jrs.5805

50. R. Esposito, R.J. Bodnar, L.V. Danyusheversusky, B. de Vivo, et al. "Volatile Evolution of Magma Associated with the Solchiaro Eruption in the Phlegrean Volcanic District (Italy)". J. Petrol. 2011. 52(12): 2431–2460. https://doi.org/10.1093/petrology/egr051

51. L.R. Moore, E. Gazel, R. Tuohy, A.S. Lloyd, et al. "Bubbles Matter: An Assessment of the Contribution of Vapor Bubbles to Melt Inclusion Volatile Budgets". Am. Mineral. 2015. 100(4): 806–823. https://doi.org/10.2138/am-2015-5036

52. E.M. Aster, P.J. Wallace, L.R. Moore, J. Watkins, et al. "Reconstructing CO_2 Concentrations in Basaltic Melt Inclusions Using Raman Analysis of Vapor Bubbles". J. Volcanol. Geoth. Res. 2016. 323: 148–162. https://doi.org/10.1016/j.jvolgeores.2016.04.028

53. P. Robidoux, M.L. Frezzotti, E.H. Hauri, A. Aiuppa. "Shrinkage Bubbles: The C–O–H–S Magmatic Fluid System at San Cristóbal Volcano". J. Petrol. 2018. 59(11): 2093–2122. https://doi.org/10.1093/petrology/egy092

Figure Captions

Fig. 1. (a) CO_2 Raman spectrum of one fluid inclusion in a peridotite from El Hierro, Canary Islands. It is characterized by: the upper and lower bands, at 1384.93 cm^{-1} and 1279.76 cm^{-1}, composing the "Fermi diad" (ν_1–$2\nu_2$); the two hot bands arising from the transitions originated due to the thermal energy of the molecules, at 1406.78 cm^{-1} and 1260.81 cm^{-1}; the $^{13}CO_2$ peak at 1367.45 cm^{-1}. The Fermi diad frequencies are shifted compared to those at ambient conditions due to the higher density of the fluid analyzed from mantle depth. b) Graphical expression of Raman densimeter empirical equations on a Δ density plot. The linear equations of Rosso and Bodnar[11] and Lamadrid et al.[19] have been not considered since they are not comparable with all the other densimeter regressions. K = Kawakami et al.;[14] Y = Yamamoto and Kagi;[15] S = Song et al.;[16] F = Fall et al.;[17] W = Wang et al.;[18] L = Lamadrid et al.[19] (c–d) Microphotographs of selected CO_2 fluid inclusions in orthopyroxene from spinel–harzburgite XML11. Black arrows indicate analyzed fluid inclusions. Δ = distance of the Fermi diad split in cm^{-1}; *d* = density; Opx = orthopyroxene.

Fig. 2. Intensities (I) versus band shape factors (BSF) of fitted CO_2 (a) upper and (b) lower bands. The horizontal and vertical dotted red lines cross into the points where the hyperboles invert their slope and represent the threshold value for selecting accurate spectra.

Fig. 3. Graphical expression of proposed densimeter equation. (a) Third order polynomial regression curve (orange) obtained by interpolating selected Δ*d* relations. (b) Regression of "microthermometric" densities (d_{micro}) versus "Raman" densities (d_{Raman}). The solid black line shows the correlation between the d_{micro} and d_{Raman}. (c) Graphical comparison of present study, R, Kawakami et al., K,[14] and Yamamoto and Kagi, Y,[15] densimeter regressions on a Δ*d* plot. Δ = distance of the Fermi diad split; *d* = density.

Fig. 4. Plots of the percent variation (%Variation) of fitted densities (Fitted d) versus Δ values, obtained after the residual bootstrapping for the equations of K, Y, and R (Figs. 4a–c; cf., Fig. 1b) and F, W, and S (Figs. 4d–f; cf. Fig. 1b). The red dotted lines represent the Δ density threshold values above which the relative error of the fitted density values is lower than 7.5%; the red fields correspond to those Δ densities below the minimum reliable values defined by the statistic thresholds. Δ = distance of the Fermi diad split.

Fig. 5. Statistical comparison of the dataset independent new empirical regressions, obtained after the residual bootstrapping for the "medium spectral resolution" equations (K, Y, and R). Δs measured by Y are used to calculate fitted densities (Fitted d) with K equation (a) and compared with Y's confidence intervals (CIs). Δs measured by K are used to calculate Fitted d with Y (b) and R (d) new equations and compared with K's CIs. Δs measured by R are used to calculate Fitted d with K equation (c) and compared with R's CIs. Red dotted line and red field as in Fig. 4; Δ = distance of the Fermi diad split. Abbreviations as in Fig. 1b.

Fig. 6. Statistical comparison of the dataset independent new empirical regressions, obtained after the residual bootstrapping for the "high spectral resolution" equations (F, W, and S; Fig. 6–c) and the "medium and the high spectral resolution" equations (Y, F, W, and S; Fig.6 d, e and f). Δs measured by (a) W and (b) S are used to calculate fitted densities (Fitted d) with F new equation and compared with the confidence intervals (CIs) of W and S, respectively. Δs measured by W are used to calculate Fitted d by S new equation (c) and compared with Ws CIs. Δs measured by (d) F, (e) W, and (f) S are used to calculate fitted densities (Fitted d) with Y new equation and, then, compared with the CI of F, W, and S, respectively. Red dotted line and red field as in Figs. 4; Δ = distance of the Fermi diad split. Abbreviations as in Fig. 1b.

Tables

Table I. Summary of the independently calculated densities (d) and Δ values of the 27 selected fluid inclusions. Homogenization temperatures (Th) are also reported.

Host	FI n°	d (g/cm^3)	Th (°C)		Δ (cm^{-1})
Opx	XML3B_120	0.37	30.5	*V*	103.44
Opx	XML3B_125	0.47	30.95	*L*	103.62
Opx	XML3B_122	0.62	29.2	*L*	103.97
Opx	XML3B_128	0.64	28.5	*L*	103.99
Ol	XML4B_112	0.68	26.5	*L*	104.07
Ol	XML4B_111	0.71	24.9	*L*	104.13
Ol	XML4B_102	0.71	24.9	*L*	104.07
Ol	XML4B_101	0.73	23.8	*L*	104.15
Ol	XML4B_109	0.73	23.6	*L*	104.17
Ol	XML4B_113	0.73	23.6	*L*	104.11
Ol	XML4B_100	0.73	23.6	*L*	104.12
Ol	XML4B_116	0.73	23.5	*L*	104.13
Ol	XML4B_110	0.76	23.2	*L*	104.23
Opx	XML3B_24	0.90	3.9	*L*	104.52
Opx	XML3B_26	0.92	2.1	*L*	104.65
Opx	XML3B_25	0.92	0.9	*L*	104.74
Ol	XML4B_16	0.94	–2.0	*L*	104.67
Opx	XML3B_28	0.94	–2.5	*L*	104.63
Opx	XML3B_23	0.95	–3.4	*L*	104.74
Ol	XML4B_12	0.95	–4.0	*L*	104.68
Opx	XML3B_27	1.02	–17.0	*L*	104.85
Ol	XML10C_8	1.04	–21.9	*L*	105.04
Ol	XML10C_13	1.05	–23.5	*L*	105.05
Ol	XML10C_10	1.05	–24.5	*L*	105.06
Opx	XML11B_6	1.06	–25.9	*L*	105.07
Opx	XML8A_19	1.07	–29.4	*L*	105.07
Opx	XML8A_17	1.08	–30.5	*L*	105.13

FI = Fluid inclusion; n° = number; Opx = orthopyroxene; Ol = olivine; V = vapor; L = liquid; Δ = distance of the Fermi diad split.

Table II. Empirical equations (orthogonal polynomial) used for residual bootstrapping.

Equation	Dataset independent new equations	Std. Error (g/cm^3)	Adj. R^2
Kawakami et al.[14]	$-0.118963\Delta^3 - 0.241733\Delta^2 + 2.359035\Delta + 0.727095$	0.02	0.998
Yamamoto and Kagi[15]	$-0.12567\Delta^3 - 0.448236\Delta^2 + 2.762602\Delta + 0.846051$	0.02	0.998
Song et al.[16]	$-0.022998\Delta^3 - 0.040964\Delta^2 + 1.260887\Delta + 0.662$	0.01	0.998
Fall et al.[17]	$-0.097391\Delta^3 - 0.183873\Delta^2 + 2.990265\Delta + 0.686497$	0.01	0.999
Wang et al.[18]	$-0.09871\Delta^3 - 0.13213\Delta^2 + 2.71578\Delta + 0.54435$	0.01	0.998
Present study	$0.031447\Delta^3 - 0.105221\Delta^2 + 1.014913\Delta + 0.844902$	0.02	0.985

Δ = distance between the Fermi diad split; Std. Error = standard error; Adj. R^2 = adjusted R^2.

Table III. Review of the analytical conditions adopted by different authors to calibrate Raman densimeter equations.

Densimeter equation	Rosso and Bodnar[11]	Kawakami et al.[14]	Yamamoto and Kagi[15]	Song et al.[16]	Fall et al.[17]	Wang et al.[18]	Lamadrid et al.[19]	Present study
Polynomial regression	Linear	Cubic	Cubic	Cubic	Cubic	Cubic	Linear	Cubic
Fluid inclusions	Synthetic H_2O–CO_2	Natural and synthetic pure CO_2	Natural and synthetic pure CO_2	Synthetic nearly pure CO_2	Synthetic H_2O–CO_2, variable salinity	Synthetic pure CO_2	Optical cell pure CO_2	Natural pure CO_2
Δ range (cm^{-1})	102.60–105.20	102.71–105.81	102.71–106.10	102.82–105.22	102.65–105.47	102.83–105.16	102.64–103.23	103.44–105.13
***d* range (g/cm^3)**	0.03–1.00	0.10–1.22	0.10 – 1.24	0.06–1.05	0.001–1.08	0.05–1.00	0.001–0.21	0.37–1.07
Equation of state	Sterner and Bodnar[37]	Pitzner and Sterner[38]	Pitzner and Sterner[38]	Angus et al.[39]	Span and Wagner[40]	Span and Wagner[40]	Span and Wagner[40]	Dusheck et al.[23]
Spectrometer	Dilor XY	Chromex 250is	Chromex 250is	Horiba HR	Horiba HR	Horiba HR	Horiba HR	Horiba HR

Laser (nm)	514.5	514.5	514.5	532.06	514.5	532.06	514.5	532.06
Slit (µm)	100	–	–	–	150	–	–	300
Dispersion grating (gr/mm)	1200	600	600	1800	2400	1800	1800	600
CCD	1024*256	1024*256	1024*256	1024*256	1024*256	1024*256	1024*256	1024*256
Spectral resolution (cm^{-1}/px)	0.84	1.5	1.5	0.3	0.3	0.43	0.575	1.66
Calibration standard	Ne lines	Naphtalene	Naphtalene	Diamond	Ne lines	Diamond and benzonitrile	Ne lines	Diamond
***d* error (g/cm^3)**	±0.02	±0.02	±0.02	±0.03	±0.035	±0.011	±0.0034	±0.015

Δ = distance of the Fermi diad split; *d* = density; – means not reported; CCD = charge-coupled device.

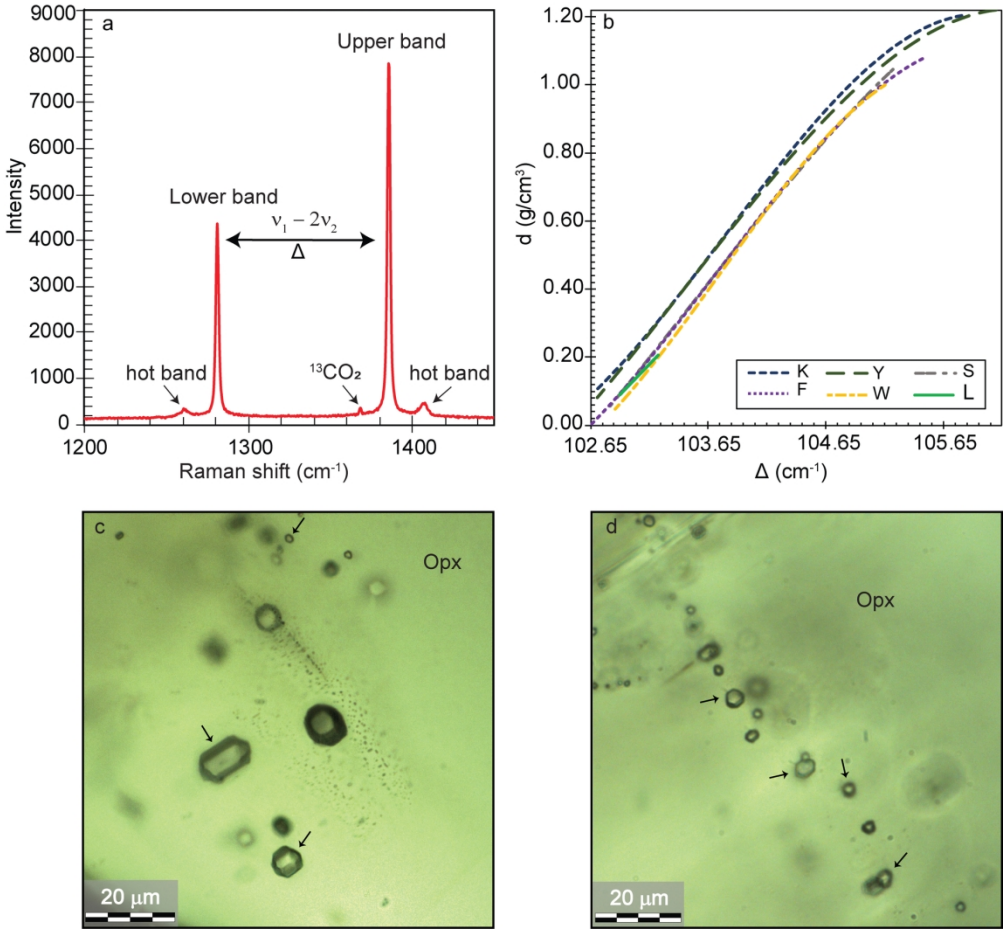

Fig.1 a) CO2 Raman spectrum of one fluid inclusion in a peridotite from El Hierro, Canary Islands. It is characterized by: the upper and lower bands, at 1384.93 cm-1 and 1279.76 cm-1, composing the "Fermi diad" (v1-2v2); the two hot bands arising from the transitions originated due to the thermal energy of the molecules, at 1406.78 cm-1 and 1260.81 cm-1; the 13CO2 peak at 1367.45 cm-1. The Fermi diad frequencies are shifted compared to those at ambient conditions due to the higher density of the fluid analyzed from mantle depth. b) Graphical expression of Raman densimeter empirical equations on a Δ – density plot. The linear equations of Rosso and Bodnar (1995) 11 and Lamadrid et al. (2017) 19 have been not considered since they are not comparable with all the other densimeter regressions. K = Kawakami et al. (2003) 14; Y = Yamamoto and Kagi (2006) 15; S = Song et al. (2009) 16; F = Fall et al. (2011) 17; W = Wang et al. (2011)18; L = Lamadrid et al. (2017) 19. c) and d) Microphotographs of selected CO2 fluid inclusions in orthopyroxene from spinel-harzburgite XML11. Black arrows indicate analysed fluid inclusions. Δ = distance of the Fermi diad split in cm-1; I = intensity in arbitrary units (a.u.); d = density; Opx = orthopyroxene.

168x156mm (300 x 300 DPI)

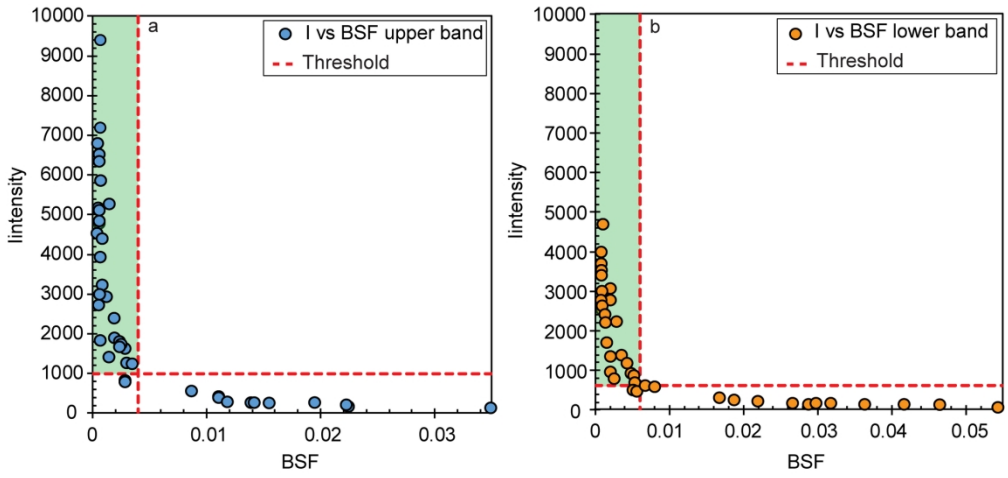

Fig.2 Intensities (I) versus band shape factors (BSF) of fitted CO2 upper (a) and lower bands (b). The horizontal and vertical dotted red lines cross into the points where the hyperboles invert their slopes and represent the threshold value for selecting accurate spectra.

179x84mm (300 x 300 DPI)

Supplementary Material

Table S1. Summary of the main characteristics of seventy-two selected fluid inclusions.

Host	FI n.°	Size (µm)	Depth (µm)	Tm (°C)	Th (°C)		*d* (g/cm^3)
Opx	XML3B_120	8	43	-56.6	30.5	V	0.37
Opx	XML3B_121	7	40	-56.6	30.92	V	0.42
Opx	XML3B_125	6	33	-56.6	30.95	L	0.47
Opx	XML3B_122	4	43	-56.6	29.2	L	0.62
Opx	XML3B_124	4	42	-56.6	29.1	L	0.63
Opx	XML3B_128	9	35	-56.6	28.5	L	0.64
Ol	XML4B_112	8	32	-56.6	26.5	L	0.68
Ol	XML4B_111	8	32	-56.6	24.9	L	0.71
Ol	XML4B_102	6	26	-56.6	24.9	L	0.71
Ol	XML4B_101	12	27	-56.6	23.8	L	0.73
Ol	XML4B_100	10	31	-56.6	23.6	L	0.73
Ol	XML4B_116	8	17	-56.6	23.5	L	0.73
Ol	XML4B_113	7	32	-56.6	23.6	L	0.73
Ol	XML4B_109	6	33	-56.6	23.6	L	0.73
Ol	XML4B_110	8	32	-56.6	23.2	L	0.76
Opx	XML8C_29	4	26	-56.6	13.0	L	0.84
Opx	XML8C_26	4	27	-56.6	8.3	L	0.87
Opx	XML8C_30	10	24	-56.6	8.9	L	0.87
Opx	XML8C_23	6	27	-56.6	7.4	L	0.88
Opx	XML8C_28	14	23	-56.6	7.8	L	0.88
Opx	XML8C_25	5	25	-56.6	5.6	L	0.89
Opx	XML8C_24	5	23	-56.6	5.6	L	0.89
Opx	XML3B_24	2	25	-56.6	3.9	L	0.90
Opx	XML3B_41	2	25	-56.6	2.0	L	0.92
Opx	XML3B_26	2.5	26	-56.6	2.1	L	0.92
Opx	XML8C_27	4	30	-56.6	0.6	L	0.92
Opx	XML3B_39	4	30	-56.6	1.0	L	0.92
Ol	XML3B_25	3.5	26	-56.6	0.9	L	0.92
Ol	XML3B_28	3	25	-56.6	-2.5	L	0.94
Opx	XML4B_16	5	39	-56.6	-2.0	L	0.94
Opx	XML4B_12	4	10	-56.6	-4.0	L	0.95
Opx	XML3B_23	2.5	23.5	-56.6	-3.4	L	0.95
Opx	XML3B_27	4	30	-56.6	-17.0	L	1.02
Opx	XML3B_42	2.5	26	-56.6	-17.1	L	1.02
Ol	XML10C_8	4	15	-56.6	-21.9	L	1.04
Ol	XML10C_13	5	13	-56.6	-23.5	L	1.05
Ol	XML10C_16	3	17	-56.6	-24.5	L	1.05
Opx	XML11B_6	6	20	-56.6	-25.9	L	1.06
Opx	XML8A_19	20	14	-56.6	-29.4	L	1.07

Opx	XML8A_17	7	14	-56.6	-30.5	L	1.08
Ol	XML11B_7	4	18	-56.7	13.0	L	0.84
Ol	XML3B_31	5	40	-56.7	8.7	L	0.87
Opx	XML11B_11	5	15	-56.9	7.5	L	0.88
Ol	XML11B_12	3.5	17.5	-56.6	5.7	L	0.89
Ol	XML4B_15	2.5	12.5	-56.6	-3.8	L	0.95
Opx	XML3A_34	3	24	-57.1	-5.5	L	0.96
Ol	XML4B_13	8	10	-56.6	-5.4	L	0.96
Ol	XML4B_14	2	16	-56.7	-7.0	L	0.97
Opx	XML3A_35	5	26	-57.0	-11.5	L	0.99
Opx	XML10C_7	4	20	-56.6	-13.0	L	1.00
Ol	XML3A_33	3.5	22	-56.9	-15.5	L	1.01
Ol	XML10C_5	3	17	-56.6	-18.3	L	1.02
Ol	XML10C_1	5	21	-56.8	-23.7	L	1.05
Ol	XML10C_3	4	21	-56.6	-24.2	L	1.05
Opx	XML11B_14	6	15	-56.6	-24.3	L	1.05
Opx	XML11B_15	6.5	8	-56.6	-24.6	L	1.05
Opx	XML10C_2	3	22	-56.7	-26.2	L	1.06
Opx	XML10C_38	4	26	-56.6	-16.5	L	1.02
Ol	XML10C_10	3	17	-56.6	-16.5	L	1.02
Opx	XML10C_1b	5	21	-56.6	-24.0	L	1.05
Opx	XML10C_3b	4	21	-56.6	-24.0	L	1.05
Ol	XML4B_17	4.5	33	-56.6	-11.9	L	0.99
Opx	XML10C_2b	3	22	-56.6	-25.0	L	1.05
Opx	XML10C_11b	3	27	-56.6	-20.3	L	1.03
Ol	XML4B_13	8	10	-56.6	-10.0	L	1.05
Ol	XML4B_115	6	14.5	-56.6	25.2	L	0.71
Ol	XML4B_117	10	23	-56.6	21.4	L	0.76
Opx	XML11B_3	5	15	-56.6	-32.5	L	1.09
Opx	XML11B_1	4	10	-56.6	-32.1	L	1.08
Opx	XML11B_4	5	9	-56.6	12.1	L	0.85
Opx	XML4B_115b	5	14.5	-56.6	25.2	L	0.71
Opx	XML4B_117b	10	23	-56.6	21.4	L	0.76

Reported densities (d) are calculated based on recorded fluid inclusions' homogenization temperatures (Th), measured by microthermometry. Final melting temperatures are also reported (Tm). FI = fluid inclusion; n° = number; Opx = orthopyroxene; Ol = olivine; V = vapor; L = liquid.

Table S2. Summary of the parameters (position, intensity and full width at half maximum) of the CO_2 Fermi diads measured after the fitting of collected CO_2 Raman spectra, and band shape factors calculated for the upper (BSF^+) and the lower (BSF^-) bands. CO_2 density (d) is also reported.

FI n.°	*d* (g/cm³)	Band⁺ (cm⁻¹)	Band⁻ (cm⁻¹)	*I*⁺	*I*⁻	*FWHM*⁺	*FWHM*⁻	*BSF*⁺	*BSF*⁻
XML3B_120	0.37	1389.41	1285.97	3208	1623	2.00	2.40	0.0006	0.0015
XML3B_121	0.42	1389.39	1285.98	799	434	2.33	2.50	0.0029	0.0058
XML3B_125	0.47	1389.73	1286.11	1734	931	2.00	2.20	0.0012	0.0024
XML3B_122	0.62	1388.80	1284.83	1314	792	2.22	2.22	0.0017	0.0028
XML3B_124	0.63	1389.15	1285.25	841	463	2.45	2.50	0.0029	0.0054
XML3B_128	0.64	1389.04	1285.05	2911	1705	2.40	2.40	0.0008	0.0014
XML4B_112	0.68	1388.31	1284.20	4576	2367	2.30	2.50	0.0005	0.0011
XML4B_111	0.71	1388.32	1284.11	4821	2477	2.35	2.30	0.0005	0.0009
XML4B_102	0.71	1388.44	1284.37	6449	3551	2.20	2.40	0.0003	0.0007
XML4B_101	0.73	1388.56	1284.38	6781	3692	2.37	2.25	0.0003	0.0006
XML4B_100	0.73	1387.99	1283.88	7156	3984	2.37	2.50	0.0003	0.0006
XML4B_116	0.73	1388.43	1284.31	6336	3406	2.37	2.40	0.0004	0.0007
XML4B_113	0.73	1388.30	1284.16	4878	2600	2.36	2.50	0.0005	0.0010
XML4B_109	0.73	1388.26	1284.09	5098	2736	2.00	2.30	0.0004	0.0008
XML4B_110	0.76	1388.16	1283.93	3902	2169	2.39	2.56	0.0006	0.0012
XML8C_29	0.84	1389.79	1285.34	276	136	3.92	4.08	0.0142	0.0301
XML8C_26	0.87	1389.60	1285.10	110	64	3.84	3.50	0.0349	0.0545
XML8C_30	0.87	1389.79	1285.24	303	144	3.60	3.86	0.0119	0.0268
XML8C_23	0.88	1389.35	1284.83	274	143	4.26	4.54	0.0155	0.0319
XML8C_28	0.88	1389.69	1285.16	347	174	3.76	3.86	0.0108	0.0222
XML8C_25	0.89	1389.45	1284.86	196	105	4.34	4.40	0.0221	0.0419
XML8C_24	0.89	1389.35	1284.75	163	89	3.64	4.16	0.0223	0.0467
XML3B_24	0.90	1386.95	1282.43	1798	888	4.06	4.56	0.0023	0.0051
XML3B_41	0.92	1389.75	1285.16	439	229	3.84	3.90	0.0088	0.0170
XML3B_26	0.92	1387.02	1282.40	1166	576	4.48	4.74	0.0038	0.0082
XML8C_27	0.92	1389.59	1284.96	272	134	3.78	3.88	0.0139	0.0290
XML3B_39	0.92	1389.88	1285.18	194	110	3.78	4.04	0.0195	0.0367
XML3B_25	0.92	1386.76	1282.03	2371	1196	4.29	4.56	0.0018	0.0038
XML3B_28	0.94	1386.77	1282.14	2869	1401	4.22	4.70	0.0015	0.0034
XML4B_16	0.94	1387.46	1282.79	1486	820	4.70	4.50	0.0032	0.0055
XML4B_12	0.95	1387.07	1282.39	5159	2724	5.06	4.80	0.0010	0.0018
XML3B_23	0.95	1386.73	1281.99	1655	901	4.50	4.60	0.0027	0.0051
XML3B_27	1.02	1386.42	1281.57	1605	849	4.70	4.60	0.0029	0.0054
XML3B_42	1.02	1389.70	1284.84	380	206	4.10	3.90	0.0108	0.0189
XML10C_8	1.04	1386.80	1281.77	9350	4688	4.40	4.52	0.0005	0.0010
XML10C_13	1.05	1387.30	1282.25	4314	2186	4.92	4.80	0.0011	0.0022
XML10C_10	1.05	1386.82	1281.76	5827	3024	4.20	4.72	0.0007	0.0016
XML11B_6	1.06	1387.98	1282.91	2669	1342	2.16	2.20	0.0008	0.0016

XML8A_19	1.07	1389.17	1284.10	1194	596	3.92	4.16	0.0033	0.0070
XML8A_17	1.08	1389.07	1283.94	1510	758	4.28	4.24	0.0028	0.0056

Red values correspond to the spectra which are not considered accurate based on the intensity and the band shape factor thresholds. FI = fluid inclusion; n° number; $Band^{+}$ = upper band position; $Band^{-}$ = lower band position; I^{+} = upper band intensity; I^{-} = lower band intensity; $FWHM^{+}$ = upper band full width at half maximum; $FWHM^{-}$ = upper band full width at half maximum.

Figure S1

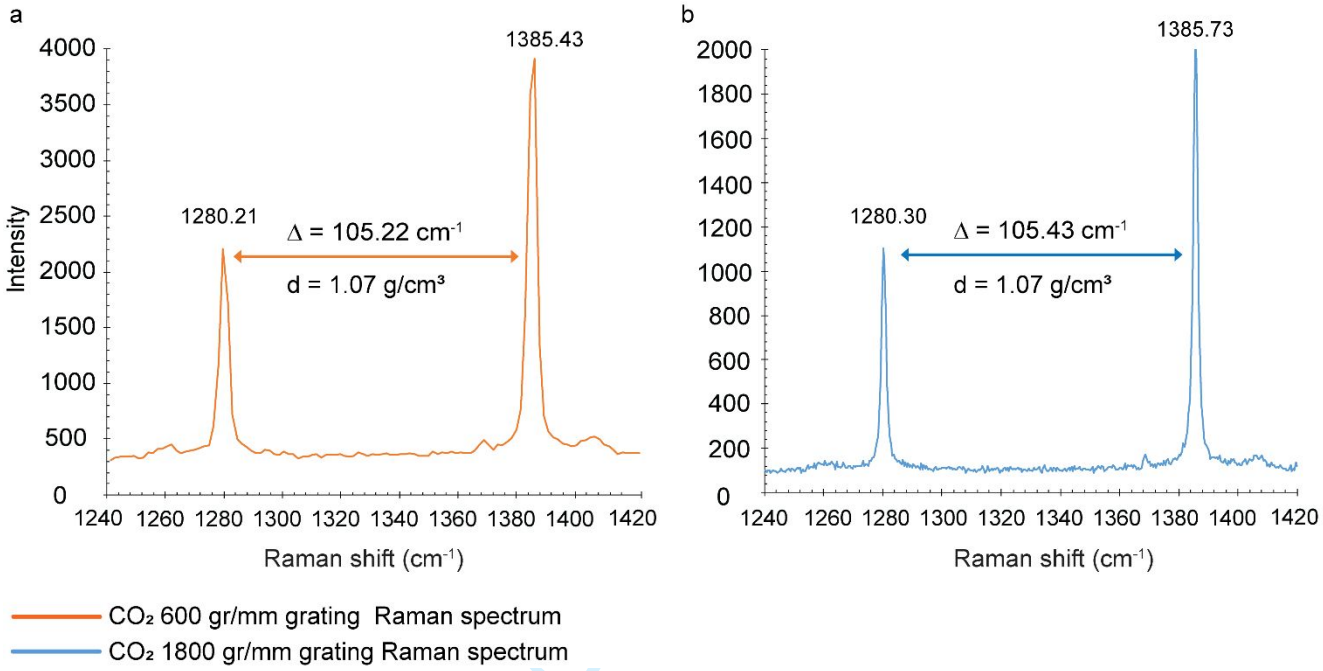

Fig. S1. Figure showing the difference between the spectra acquired with the 600 (orange) and the 1800 (blue) gr/mm grating of one CO_2 fluid inclusions of the dataset, having density of 1.07 g/cm^{-1} (F.i. n° XML8A_19). Spectra have been acquired in the Raman laboratory at the Università of Milano – Bicocca. Panel a) shows the F.i. spectrum acquired with the 600 gr/mm grating, with the upper and lower bands positions (1280.21 and 1385.43 cm^{-1}, respectively) corresponding to a distance of the Fermi diad split (Δ) of 105.22 cm^{-1}. Panel b), instead, shows the same F.i. spectrum acquired with the 1800 gr/mm grating. The upper and lower bands central positions are 1385.73 and 1280.30 cm^{-1}, respectively, corresponding to a Δ value of 105.43 cm^{-1}.

Figure S2

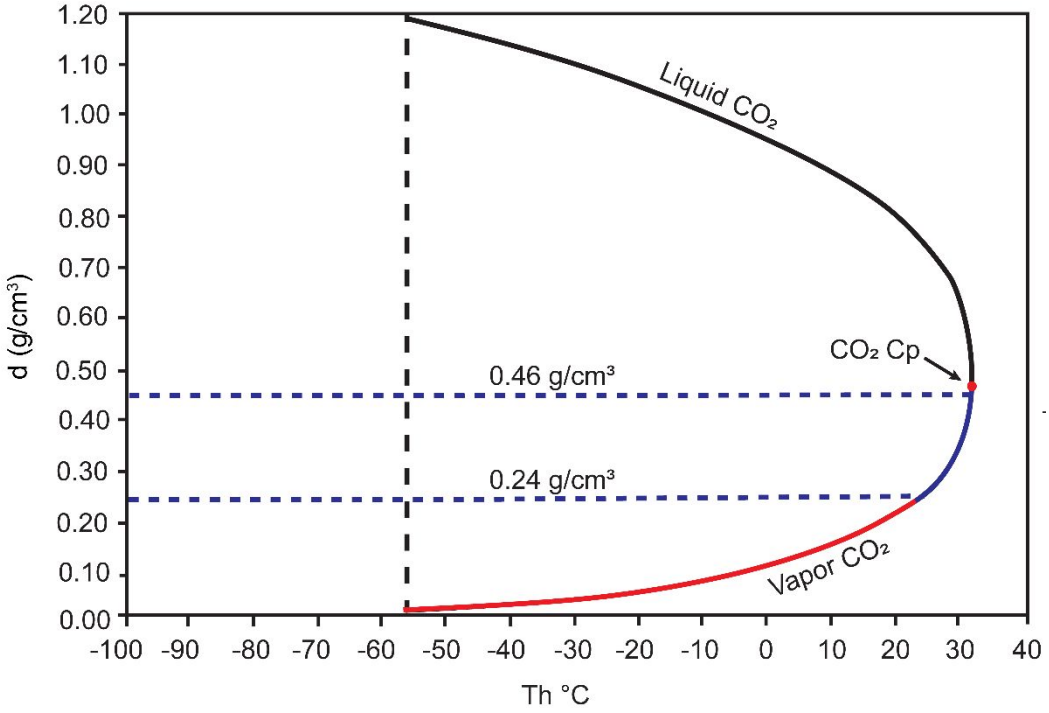

Fig. S2. CO_2 density (*d*) versus homogenization temperature (Th) plot (modified after Van den Kerkhof and Thiery, 2001).1 The blue dotted lines correspond to the highest and the lowest threshold densities (i.e, 0.46 g/cm^3, and 0.24 g/cm^3, respectively) set after the residual bootstrapping. These define the Th – d interval (blue solid curve) comprising the thresholds set for all the other equations, corresponding to CO_2 fluids homogenizing to the vapor phase. The red dot corresponds to the CO_2 critical point (Cp, d = 0.466 g/cm^3 at 31.1 °C). The solid black curve defines the Th – d interval where CO_2 homogenizes to the liquid phase, while the red one the interval where CO_2 homogenizes to the vapor phase, below the threshold densities.

References

1. A. Van den Kerkhof, R. Thiery. "Carbonic inclusions". Lithos. 2001. 55(1-4): 49-68.

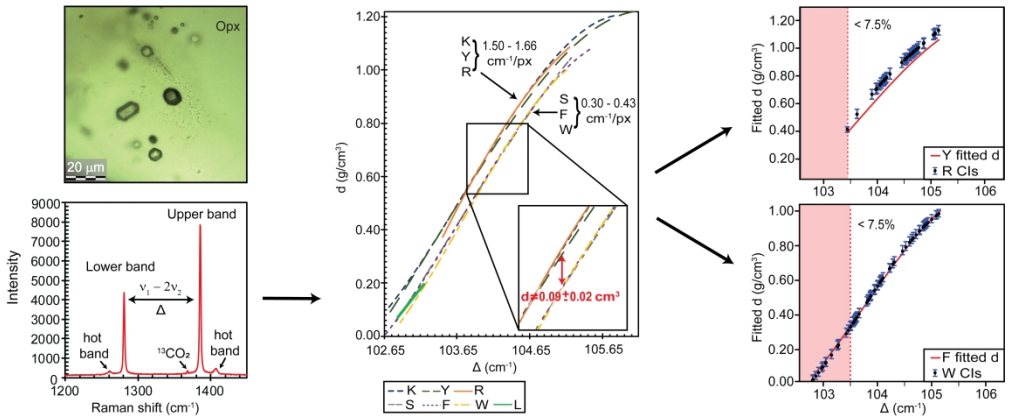

452x188mm (300 x 300 DPI)